Tailoring photoactivity of polymeric carbon nitride via donor-π-acceptor network

Toshali Bhoyar [a], Dong Jin Kim [b], B. Moses Abraham [c], Surendar Tonda [d], Nilesh R. Manwar [e], Devthade Vidyasagar [a],[*],[1], Suresh S. Umare [a],[*]

[a] Materials and Catalysis Laboratory, Department of Chemistry, Visvesvaraya National Institute of Technology (VNIT), Nagpur 440010, India
[b] School of Energy and Engineering, Kyungpook National University, Buk-gu, Daegu 41566, Republic of Korea
[c] Department of Chemical Engineering, Indian Institute of Technology, Kanpur 208016, India
[d] Department of Environmental Engineering, Kyungpook National University, Buk-gu, Daegu 41566, Republic of Korea
[e] Department of Chemistry, Institute of Chemical Technology (ICT), Mumbai 400019, India

ARTICLE INFO

ABSTRACT

Molecular doping approach can effectively modulate the charge transfer kinetics of polymeric carbon nitride (PCN) photocatalyst. Herein, we show that doping of PCN with a strong electron-withdrawing 2,3-diaminopyridine (DAP) induces the formation of donor-π-acceptor (D-π-A) network. As formed D-π-A type network demonstrated a photocatalytic hydrogen production activity of 6.56 mmolg^{-1} h^{-1}, which is 4.5-times greater than the pure PCN. The optoelectronic features characterized by spectroscopic techniques indicate rapid separation of photoexcited charge carriers and extended light-harvesting ability of DAP-doped PCN. Further, the theoretical analysis revealed that DAP-doped PCN has near-ideal hydrogen adsorption free energy of − 0.11 eV, which supports the excellent hydrogen production performance. Importantly, the hydrogen production activity demonstrated here outperforms several state-of-art molecular-doped PCN-based catalysts. This study sheds light on the effective production of PCN-based D-π-A networks using conjugated heterocyclic compounds.

1. Introduction

Metal-free polymeric carbon nitride (PCN) photocatalysts are powerful oxidative semiconductors with appropriate energy levels for hydrogen evolution,[1] CO$_2$ reduction,[2] and N$_2$ fixation,[3] as well as for detoxification of organic pollutants [4]. PCN-related materials are promising alternatives to the industrially used catalysts, because of their easy synthesis, strong redox ability, thermochemical robustness, and benign metal-free composition[5]. However, the photocatalytic performance of PCN is impeded by various factors. The major constraints of PCN are limited visible-light response (< 460 nm), rapid recombination of photoexcitons, moderate surface area, and sluggish reaction kinetics [6]. There are consistent efforts to improve the surface area, minimize charge recombination, and expand the optical response of PCN-related materials. In particular nanostructure engineering,[7] hetero-/homojunction approach[8], and metal/non-metal or molecular doping [9] are well-known strategies to alter the photophysical properties of bulk PCN.

Among these, molecular doping is a unique metal-free approach to adjust the molecular and optical band structure by introducing a selective organic moiety into the PCN skeleton. To date, a plethora of aromatic organic moieties are introduced into the PCN core network. For instance, pyridine,[10] thiophene,[11] benzene, and its derivatives[12, 13] are intentionally doped into the PCN network to modify and uplift its core photocatalytic activity. In this regime, our group previously incorporated aromatic phenyl moiety and thiophene into the PCN skeleton and demonstrated the elevated photoactivity for aromatic molecule-grafted PCN, resulting from the modified band structure and charge-carrier dynamics[14]. In continuation of our efforts to utilize aromatic π-deficient organic moieties as a dopant for PCN, we identified pyridine moiety as a suitable target molecule to incorporate in the PCN network. Pyridine has a strong electron attraction ability and delocalized π-electrons over the aromatic ring due to the inductive effect of the nitrogen atom, which makes it a π-deficient molecule. Doping of pyridine or its derivatives into the PCN triazine network constructs a donor- π-acceptor (D-π-A) type configuration because of the difference in

---

electron affinities of contributing rings. Consequently, the formation of D- π-A type configuration induces intramolecular charge transfer (ICT) between donor and acceptor units, driving the electrons on the highest occupied molecular orbital (HOMO) of donor unit to the lower unoccupied molecular orbital (LUMO) of acceptor unit. As a result, electrons are accumulated on the acceptor, while the holes are left on the donor units featuring a facile separation of photoinduced charge carriers. Moreover, a new low-energy ICT absorption band is likely to appear in D- π-A networks, which extends the light absorption to a longer wavelength[10,15]. For instance, D-π-A type PCN synthesized using 2-aminobenzothiazole as an acceptor unit exhibited facile separation of charge carriers owing to the ICT phenomena [16]. A similar strategy was employed to enhance the photocatalytic hydrogen generation of PCN by incorporating π-deficient aromatic molecule creatinine into the PCN framework.[17] Besides, several other π-deficient aromatic molecules such as 2,4-diaminopyrimidine,[18] 2,5-dibromopyrazine,[19] and trimesic acid,[20] have been studied to form D-π-A type PCN, with greatly improved photocatalytic performance. These π − conjugated aromatic moieties show a synergistic effect by extended visible light absorption, exposed surface-active sites, and increased charge carrier mobility by promoting separation of photoexcitons. As a result, the constructed D-π-A type PCN structures demonstrates high photocatalytic activity.

In this work, we show the doping effect of 2,3-diaminopyridine (DAP) into the PCN framework via the thermal copolymerization process. The DAP is a π-electron-deficient nitrogenous compound with two amino groups which enable the copolymerization of DAP with urea and melamine to form DAP-doped PCN. The pyridine moiety with a strong electron-accepting ability acts as an electron acceptor while the heptazine tectonic unit of PCN act as an electron donor forming a unique D-π-A type configuration. Henceforth, copolymerization of PCN with π-electron-deficient DAP promotes the facile separation of charge carriers, extends visible light absorption, and exposes a large active surface area, which enabled a 4.5 times increment in photocatalytic hydrogen evolution ability for DAP-doped D-π-A type PCN than the bare undoped PCN.

2. Experimental section

2.1. Chemicals and materials

Urea (99%) was purchased from Merck (Mumbai, India). Melamine (99%) was purchased from Sigma Aldrich (USA). 2,3-diaminopyridine ($C_5H_7N_3$, 95%) was purchased from Sigma Aldrich (Bangalore, India). Potassium bromide (KBr), triethanolamine (TEOA), indigo carmine (IC), acid violet-7 (AV-7), malachite green (MG), methylene blue (MB), and *p*-benzoquinone (*p*-BQ) were purchased from Sigma Aldrich (USA). Rhodamine B (RhB) was purchased from the British Drug House LTD. (BDH, England). Tetracycline hydrochloride (TCH) was purchased from Tokyo Chemical Industry (TCI, India). Ammonium oxalate was purchased from Merck (Mumbai, India). Isopropyl alcohol was purchased from Merck (Mumbai, India). All the chemicals were used as purchased without further purification.

2.2. Preparation of DAP-doped D-π-A type PCN network

The π − aromatic 2,3-diaminopyridine (DAP) doped polymeric carbon nitride (PCN) was prepared by the thermal copolymerization process. In brief, different amount of DAP (5, 10, or 20 mg) and urea (10 g) were thoroughly grinned together to obtain a homogeneous mixture. The homogeneous mixture was then transferred to a silica crucible, and a thin layer of melamine (1 g) was applied to the top surface of the mixture to reduce thermal decomposition of products. The composition mixture was then annealed at 550 °C for 2 h in static air. The resulting solid product was ground into fine powder after natural cooling and labelled as *x*DAPCN (where *x* denotes the amount of DAP in mg). Alternatively, the *x*DAPCN catalyst was prepared by following the same

approach, without melamine protection layer, but any yield was not achieved. The reaction in air atmosphere induced quick evaporation of precursor mixture. Hence, to avoid rapid evaporation and promote yield of reaction, melamine thin layering approach was employed according to our previous report [14]. For comparison, the bulk polymeric carbon nitride (PCN) was prepared by following the same approach without adding DAP as a dopant.

2.3. Photocatalytic H_2 production measurement

The hydrogen evolution measurement was performed in accordance with the previous report at room temperature and atmospheric pressure [21]. In brief, 4 mg catalyst was dispersed in 40 mL of the aqueous solution containing 10 vol% triethanolamine (TEOA) as a sacrificial agent in a quartz reactor via ultrasonication for 10 mins and then Argon gas was purged for 20 mins to evacuate the reactor from oxygen creating an inert atmosphere. The Pt co-catalyst (2 wt%) was deposited in-situ on the surface of catalyst by reducing H_2PtCl_6 using 300 W Xe lamp for 60 mins. The reaction mixture was then illuminated with a 300 W Xe lamp with a 420 nm cut-off filter. After illumination, 500 μL gas was sampled at regular intervals of time and analyzed using gas chromatography (GC-2010, Shimadzu) equipped with a thermal conductivity detector (TCD), and Carboxen-1010 PLOT capillary column was used with helium as a carrier gas. The apparent quantum yield (AQY) of the catalyst was measured using the same light source equipped with 420 nm band pass filter (20BPF10–420, Newport). The detailed AQY calculation can be found in the supplementary information.

2.4. Photocatalytic degradation experiment

The dye degradation experiment was performed by dispersing 100 mg catalyst in 100 mL rhodamine B (RhB) solution of concentration 10 mgL^{-1}. The dispersion mixture was stirred for 30 min before illumination in dark to achieve adsorption-desorption equilibrium. Then the reaction mixture was illuminated with visible light in a reaction chamber equipped with LED lamps (60000–65000 lx). After every 5 min, sample aliquots were collected, centrifuged, and then analyzed using a UV-Vis spectrophotometer at 554 nm. The degradation of dyes indigo carmine (IC), acid violet 7 (AV-7), malachite green (MG), and methylene blue (MB) of concentration 10 mgL^{-1} was conducted by following the same procedure. For, tetracycline hydrochloride (TCH) degradation experiment, 50 mg catalyst was dispersed in 50 mL TCH solution (20 mgL^{-1}) and stirred in dark for 30 min similar to dye degradation experiments. The concentration of samples aliquots after visible light irradiation was recorded at an interval of 10 min using UV-Visible spectrophotometer at 357 nm.

2.5. Density functional theory calculations

First principle calculations were performed through plane-wave basis using the Vienna Ab Initio Simulation Package (VASP) under periodic boundary conditions. The projected augmented wave (PAW) formulism is employed to treat the valence orbitals of the relevant atomic species [22]. The generalized gradient approximation (GGA) is used to describe the exchange-correlation interactions, which is parameterized by the Perdew-Burke-Ernzerhof (PBE) method [23]. A kinetic energy cutoff of 500 eV is used for the plane wave expansion in the reciprocal space. The convergence thresholds were set to 0.01 eV $Å^{-1}$ for the atomic force and 10^{-5} eV for the total energy, respectively. For the geometry optimizations and electronic structure calculations, Monkhorst-Pack k-point grid $5 \times 5 \times 1$ and $9 \times 9 \times 1$ was considered respectively, to discretize the Brillouin-zone integration. To avoid the artificial interactions between periodic images, a vacuum layer of 20 Å was applied in the z-direction. The Grimme's DFT-D3 correction method is incorporated to describe the long-range interactions. Since the conventional DFT formalism typically underestimates the band gap values,

[24] we employed more accurate and expensive Heyd-Scuseria-Ernzerhof (HSE) hybrid functional to make sure that the obtained bandgaps are accurate. The hydrogen adsorption free energy ΔG_H on the studied system was computed using the equation;.

$$\Delta G_H = \Delta E_H + \Delta E_{ZPE} - T\Delta S_H \tag{1}$$

where ΔE_H, ΔE_{ZPE}, and ΔS_H are the changes in adsorption energy of hydrogen atoms, zero-point energy, and entropy absolute temperature (T = 300 K), respectively. For hydrogen adsorption, the term ($\Delta E_{ZPE} - T\Delta S_H$) is generally taken as + 0.24 eV [25]. In Eq. 1, ΔE_H is given by;

$$\Delta E_H = E_{(surface+H)} - E_{(surface)} - 1/2\, E_{H_2} \tag{2}$$

where $E_{(surface+H)}$ is the total energy of hydrogen atom on surface, and $E_{(surface)}$ and E_{H_2} indicates the total energies of pure surface and hydrogen gas, respectively. To understand the electron distribution, we computed the HOMO and LUMO energy levels of the optimized PCN and DAPCN structure using B3LYP/6–31 G(d,p) level of theory via optimally tuned ωB97XD (OT-ωB97XD) functional.

3. Results and discussion

3.1. Phase and structural property analysis

The crystal structure of the as-prepared PCN powder analyzed by the powder X-ray Diffraction (XRD) displayed two diffraction peaks at 2θ values of 13.23° and 27.55° indexed to (100) and (002) planes respectively (Fig. 1a). The (100) plane is related to the repeated packing of tris-triazine units, while the (002) plane corresponds to the graphite-like interlayer stacking (d = 0.32 nm), signifying the formation of graphitic carbon nitride phase [1]. The XRD pattern of DAP shown a number of sharp diffraction peaks signifying its crystalline nature

(Fig. S1). In comparison, the XRD pattern of DAP-doped optimized composition 10DAPCN shows graphitic phase diffraction peaks as that of PCN with an absence of diffraction peaks corresponding to DAP, indicating the retention of core PCN crystal structure post DAP doping. However, the (002) peak in DAP-doped PCN is broad and highly intense than the undoped PCN. The increase in peak intensity is likely from the removal of some specific interlayered atoms, which leads to increased intensities [26]. Moreover, the corresponding FWHM value increased from 0.805 in PCN to 0.851 for 10DAPCN, indicating a disordered triazine framework [27]. This observation hypothesizes the molecular doping of DAP into the triazine network of PCN.

We then examined the effect of DAP doping on the carbon environment of PCN using solid-state ^{13}C cross-polarization magic angle spinning (CP-MAS) nuclear magnetic resonance (NMR) spectroscopy. The solid-state ^{13}C CP-MAS NMR spectrum of undoped PCN shown two types of carbon signals at chemical shift values of 164.9 and 156.5 ppm corresponding to sp^2 bonded carbon atoms in NH$_2$-C(N)$_2$ (C$_1$) and C-(N)$_3$ (C$_2$) carbons of the heptazine ring, respectively (Fig. 1b) [28]. The solid-state ^{13}C CP-MAS NMR spectrum of DAP shown five featured signals at 149.6, 135.8, 129.4, 120.6, and 112.2 ppm corresponding to aromatic carbon atoms in DAP. Analogously to PCN, the solid-state ^{13}C CP-MAS NMR spectrum of 10DAPCN shown the characteristics peaks of PCN along with new weak low intensity signals (*) centred at 148.2, 141.6, 129.6, 117.9, and 106.1 ppm, corresponding to the aromatic bonding of DAP moiety,[29] suggesting the existence of pyridinic rings in PCN framework. Notably, the new signals shown slight upfield and downfield chemical shift compared to that of pristine DAP. The shift in the characteristics signals indicates the formation of new chemical bonds between DAP and heptazine core during polymerization process, which induced a change in carbon environment. In addition, few low intensity signals were seen around 100–90 ppm, which are likely from the existence of sp^3-hybridized carbon in the heptazine core.
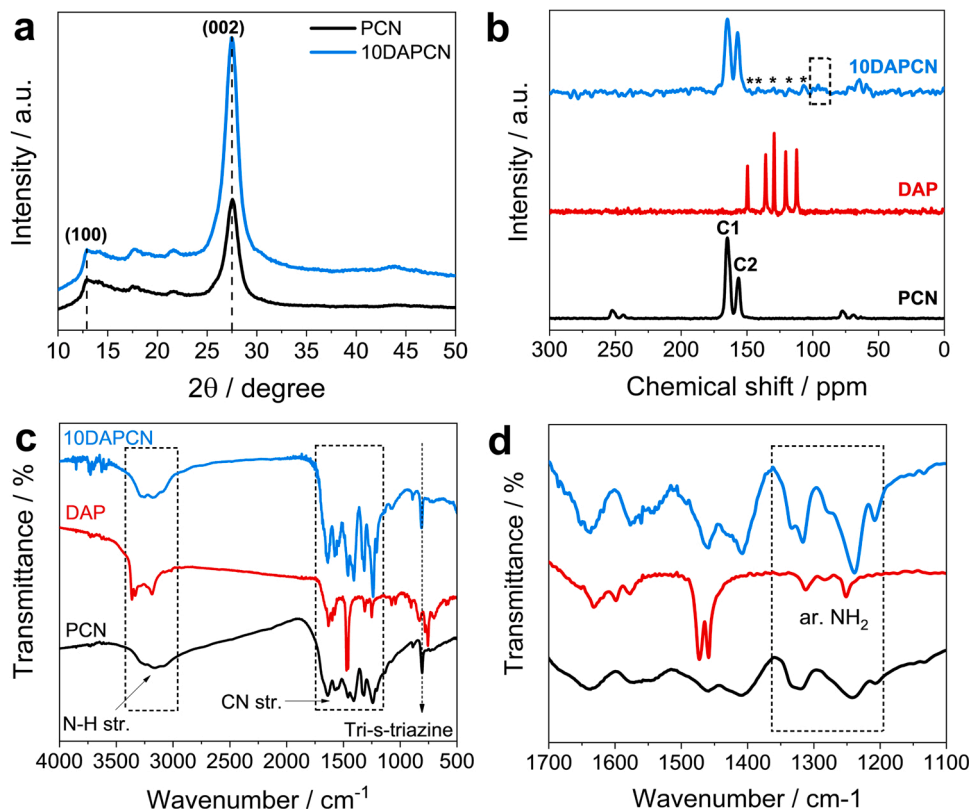
Fig. 1. Phase and structural characteristics of DAP-doped PCN. (a) X-ray diffraction (XRD) pattern of 10DAPCN demonstrating disordered PCN structure, (b) solid-state ^{13}C cross-polarization magic angle spinning (CP-MAS) nuclear magnetic resonance (NMR), and (c and d) Fourier transform infrared (FT-IR) spectrum of PCN, DAP, and 10DAPCN catalyst showing characteristic features of DAP moiety.

Furthermore, the C_2 signal intensity in 10DAPCN is relatively larger than undoped PCN and the C_2/C_1 signal ratio increased from 0.5 to 0.8, which indicates the drastic change in the local carbon environment of PCN due to the additional DAP moiety. These distinctive carbon features in 10DAPCN further confirm the successful incorporation of DAP into PCN conjugated network.

The Fourier transform infrared (FT-IR) spectrum of PCN exhibits characteristics stretching vibrations of aromatic CN heterocycles ca. 1200–1700 cm^{-1} and breathing mode of tri-s-triazine rings at 807 cm^{-1} (Fig. 1c) [30]. The broad vibrational band in the range 3000–3400 cm^{-1} is attributed to the N-H stretching vibration of uncondensed terminal amine groups on the surface. Whereas, the DAP-doped PCN shown all the vibrational peaks of PCN indicating that carbon nitride structure is retained even after doping with DAP. Besides, most of the vibrational peaks of DAP overlaps with that of PCN and therefore exhibits increased peak intensity. Nevertheless, aromatic C=C stretching vibration of pyridine molecule featuring at ~1577 cm^{-1} was seen in DAP-doped PCN catalyst (Fig. 1d) [29]. In addition, C-N stretching vibration of aromatic amine groups of DAP ca. 1335–1250 cm^{-1} are located in the DAP-doped PCN catalyst that confirms the presence of DAP moieties in the doped PCN catalysts.

The chemical composition and the elemental state of PCN and optimized 10DAPCN catalyst analyzed by the X-ray photoelectron spectroscopy (XPS) shows the existence of carbon, nitrogen, and oxygen elements on the surface (Fig. 2a). The fitted high-resolution C1s spectrum of PCN catalyst shows three main peaks centered at a binding energy of 284.80, 286.19, and 287.99 eV, which corresponds to adventitious C-C carbon, C-NH$_x$ ($x = 1, 2$), and N-C=N linkage in the PCN framework, respectively [31,32]. Interestingly, the C1s spectrum of DAP-doped 10DAPCN catalyst also exhibits three peaks but are slightly shifted to higher binding energy values 284.80, 286.75, and 287.96 eV (Fig. 2b). Furthermore, in comparison to pristine PCN, the percentage peak area of N-C=N to the total peak area of carbon atoms in 10DAPCN decreases from 93.93% to 75.39% (Table S1). Whereas, the peak area percentage of C-NH$_x$ linkage increases from 1.29% to 17.88%, and adventitious C-C increases from 5.55% to 8.67%. These findings suggest that after doping with DAP, additional C-NH$_2$ groups are introduced in the PCN framework and C=C bonds of DAP are also present in the 10DAPCN catalyst. The increase in the peak area of C-NH$_x$ linkage is likely from the contribution of C-NH$_2$ groups of the DAP in the 10DAPCN

catalyst. The high-resolution N1s spectra of PCN is deconvoluted to three peaks positioned at 398.40, 399.09, and 400.87 eV assigned to C-N=C (sp^2 hybridize nitrogen atom in the heptazine rings), N-(C)$_3$ (sp^3 hybridized tertiary bridging nitrogen), and C-NH$_x$ ($x = 1, 2$) (sp^3 hybridize edge amino groups) linkage, respectively (Fig. 2c) [31]. In contrast, the N1s spectrum 10DAPCN exhibits four peaks of which three peaks at 398.43, 400.08, and 401.00 eV are consistent with the PCN. Notably, the fourth peak centered at 397.1 eV with 13.02% of the total N-peak area can be attributed to pyridinic N-atom of DAP-doped PCN [33]. The high resolution O1s spectrum of PCN and 10DAPCN is fitted with a single peak at binding energy 532.61 and 533.87 eV, respectively (Fig. S2). The peak is assigned to the adsorbed water molecules on the surface. Furthermore, the total percentage of C1s atom decreased from 41.28% to 38.53% and N1s atom increased from 58.72% to 61.47% for 10DAPCN (excluding O1s). All these findings indicate successful incorporation of DAP in PCN network.

3.2. Optical properties and microstructure analysis

The alterations in optoelectronic properties of DAP-doped PCN catalyst were then studied by ultraviolet-visible diffused reflectance spectroscopy (UV-DRS). The DRS spectrum of the yellow-colored pristine PCN shown an absorption edge at 450 nm, that arises from the $\pi - \pi *$ electronic transitions in the conjugated heptazine rings (Fig. 3a) [34]. Remarkably, DAP incorporated PCN shown a color change from yellow to brown-orange with a significant redshift, indicating the extension of π-conjugated system induced by aromatic pyridine moieties [35]. A closer inspection of the optical spectra illustrated the presence of distinct low energy mid-gap states other than $\pi - \pi *$ electronic transitions. In addition, all the DAP-doped PCN samples shown an expanded absorption tail (Urbach tail) and shoulder peak in the wavelength range from 430 to 650 nm which is ascribed to the intrinsic n-π * electronic transition. The existence of the n-π * transition, which is typically forbidden in PCN due to perfectly symmetric and planar units, indicates the formation of the asymmetric planar structure of DAP-doped PCN [36]. This transition is due to the D-π-A type intramolecular charge transfer (ICT) band, where electronic transitions occur from the HOMO of donor (heptazine) units to the LUMO of the acceptor (DAP) units owing to its high electron affinity [37]. The Urbach tail arises due to localized electronic defects states within bandgap and the
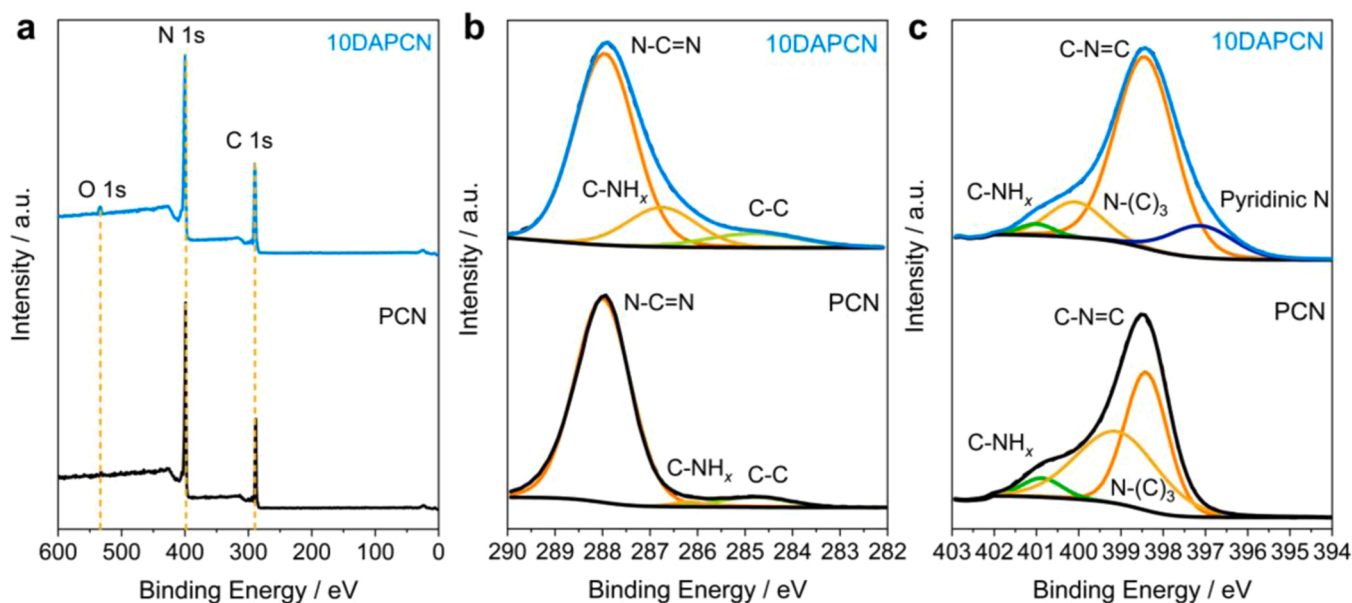
Fig. 2. Chemical composition and elemental state analysis. X-ray photoelectron spectroscopy (XPS) (a) survey spectrum, high resolution (b) C1s, and (b) N1s spectrum of PCN and 10DAPCN catalyst.
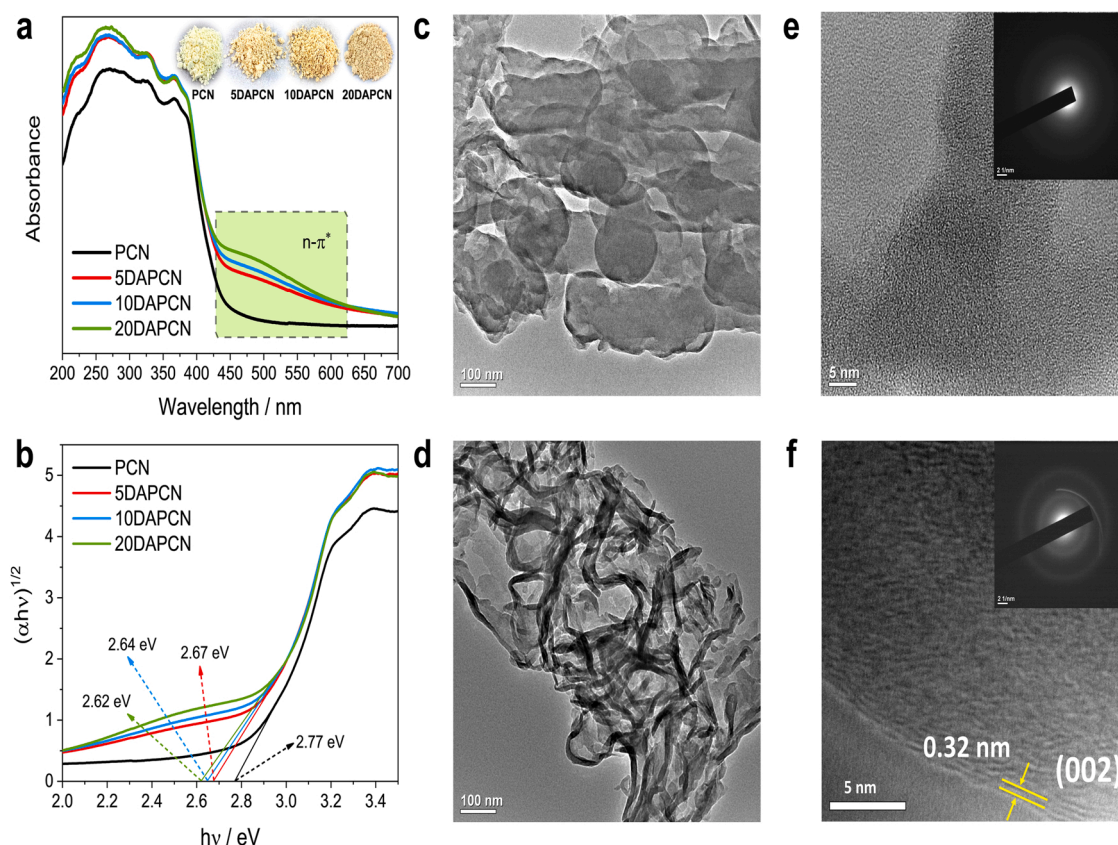
Fig. 3. Optical response and microstructure analysis. (a) UV-Visible diffuse reflectance (UV-DRS) spectra, and (b) plots of transformed Kubelka-Munk function vs photon energy for PCN and DAP-doped PCN catalysts with various amounts of DAP, (c and d) transmission electron microscopy (TEM) images, and (e and f) high-resolution transmission electron microscopy (HRTEM) images of PCN and 10DAPCN (the corresponding selected area electron diffraction pattern (SAED) is given in the inset).

energy of the band tail (Urbach energy) can be estimated by Urbach plot using Urbach Empirical rule (Eq. 3);

$$a = a_0 exp\left(\frac{h\nu}{E_u}\right) \tag{3}$$

where α is absorption coefficient, α_0 is constant, and E_u denotes Urbach Energy [38]. The E_u calculated for 10DAPCN catalyst is 0.13 eV, higher than that of PCN (0.11 eV) (Fig. S3a and b). The increase in Urbach energy is ascribed to the disordered crystal structure in agreement with the XRD analysis. The mid-gap state energy of the catalyst PCN and 10DAPCN calculated from the Kubelka-Munk (K-M) plot are 2.15 and 2.06 eV, respectively (Fig. S3c and d). Furthermore, the bandgap of the catalyst PCN and 10DAPCN estimated from the K-M plot are 2.77 and 2.64 eV, respectively (Fig. 3b) [39]. The extended visible light absorption, narrow bandgap, and high mid-gap state energy imply that the catalyst effectively harvests more visible light.

The morphology and microstructural features of PCN after DAP doping was examined by field emission scanning electron microscopy (FE-SEM) and transmission electron microscopy (TEM). The FESEM image of pure PCN displayed a typical bulk sheet like morphology with limited access to the surface-active sites (Fig. S4a). The FESEM image of the 10DAPCN catalyst, on the other hand, displayed tubular type-microstructures made-up of few-layers of carbon nitride (Fig. S4b). We believe that the steric effect of terminal pyridinic groups in the 10DAPCN network drives the few-layered tube-type morphology. These tubular morphologies can originate from the initial wrapping of few layers of PCN around an axial dislocation in self-perpetuating steps; exposing a large surface-active sites indispensable for surface photo-catalytic reactions. The TEM image of pure PCN shows a nanolayered graphite-like packed structure (Fig. 3c). In equivalent, the DAP-doped PCN exhibits change from the typical nanosheets to weakly ordered porous wrinkled nanostructure (Fig. 3d). The appearance of such weakly ordered microstructure is attributed to the formation of a cross-linked linear network and the evolution of NH₃ during the pyrolysis of the precursors. The high-resolution transmission electron microscopy (HRTEM) image of PCN does not exhibit lattice fringes inferring poor crystallinity of PCN (Fig. 3e). Nevertheless, 10DAPCN shows lattice fringes with a *d*-spacing of 0.32 Å, which corresponds to the (002) plane of PCN (Fig. 3f). These notable microstructural features further evident positive doping of PCN with DAP molecule and alterations in the crystal structure of PCN.

The thermal stability and polymerization steps of the constructed network is analyzed by thermogravimetric analysis (TGA) under N₂ atmosphere at the ramping rate of 10 °C/min (Fig. S5a). The TGA curve of urea shows that the decomposition starts with melting at 130 °C and decomposition into biuret at 230 °C with the liberation of ammonia between 230 and 250 °C (~3 wt%) (Fig. S5b). Besides, cyanuric acid gets formed in the first decomposition step which gets decomposed at 350 °C. During the decomposition of cyanuric acid, more stable compounds with high decomposition temperatures such as ammelide, ammeline, and melamine are formed [40]. These stable compounds decompose at T > 350 °C in the final step completing the decomposition of urea into carbon and nitrogen gas. The TGA curve of DAP demonstrates melting at 120 °C and decomposition at 210 °C (Fig. S5c). However, urea + DAP (U-DAP) starts melting at 120 °C (matching the melting temperature of DAP) and thermal decomposition at 217 °C (Fig. S5d). In U-DAP, the liberation of ammonia takes place between 217 and 237 °C with nearly 12% weight loss. The excessive weight loss compared to urea is due to the amino groups of DAP. Afterward,

transformation at 329 °C leads to complete weight loss of U-DAP at 530 °C, which is lower than that of urea. The low transformation and decomposition temperature signify the formation of intermediates with low thermal stability. These results indicate that the polymerization pathway is altered in U-DAP to form DAPCN structure. Further, the TGA curve of PCN and 10DAPCN shows initial weight loss up to 200 °C, which is due to the surface absorbed oxygen and other volatile impurities adsorbed on the sample surface. The PCN remained stable up to 500 °C and the structure starts collapsing completely at 750 °C (Fig. S5e). Perhaps, slight weight loss is observed at nearly 240 °C for 10DAPCN matching decomposition temperature DAP moiety (Fig. S5f). This is due to the presence of uncondensed DAP into the 10DAPCN network structure. Above 240 °C, 10DAPCN remains stable till 500 °C after which thermal deformation leads to thermal decomposition. Notably, 10DAPCN leaves 5% residual carbon above 715 °C, which might be due to the DAP moieties that form carbon deposits at a higher temperature.

A plausible copolymerization mechanism for the formation of D-π-A type network is illustrated in Scheme 1. Initially, thermal ammonolysis of urea with two amino groups of DAP molecule forms an intermediate urea-DAP network. The repetitive reaction of urea-DAP intermediate

with urea moieties forms a carbonyl-containing heterocyclic compound, which then undergoes thermal amination. Following the continuous polymerization reaction with melamine, heterocycle liberates NH_3 to yield a heptazine-based distorted PCN network as a stable powder. As discussed in the previous section, the conjugated polymeric distorted DAPCN structure can have an extra aromatic pyridine moiety that acts as a strong electron-acceptor, due to its high electron affinity, while heptazine tectonics serves as electron donor units. The synergistic assembly of pyridine and heptazine units enables the formation of the D-π-A type network.

3.3. Photocatalytic performance

The photocatalytic performance of D-π-A type PCN catalyst was assessed by hydrogen generation via water splitting reaction and degradation of organic contaminants. The photocatalytic hydrogen evolution experiment was performed under visible-light illumination ($\lambda > 420$ nm) in the presence of TEOA as sacrificial agent and Pt as co-catalyst. After four hours of visible light irradiation, the pristine PCN generated 5.82 mmolg^{-1} of hydrogen gas. Interestingly, the DAP-doped DAPCN based catalysts have shown significantly improved hydrogen
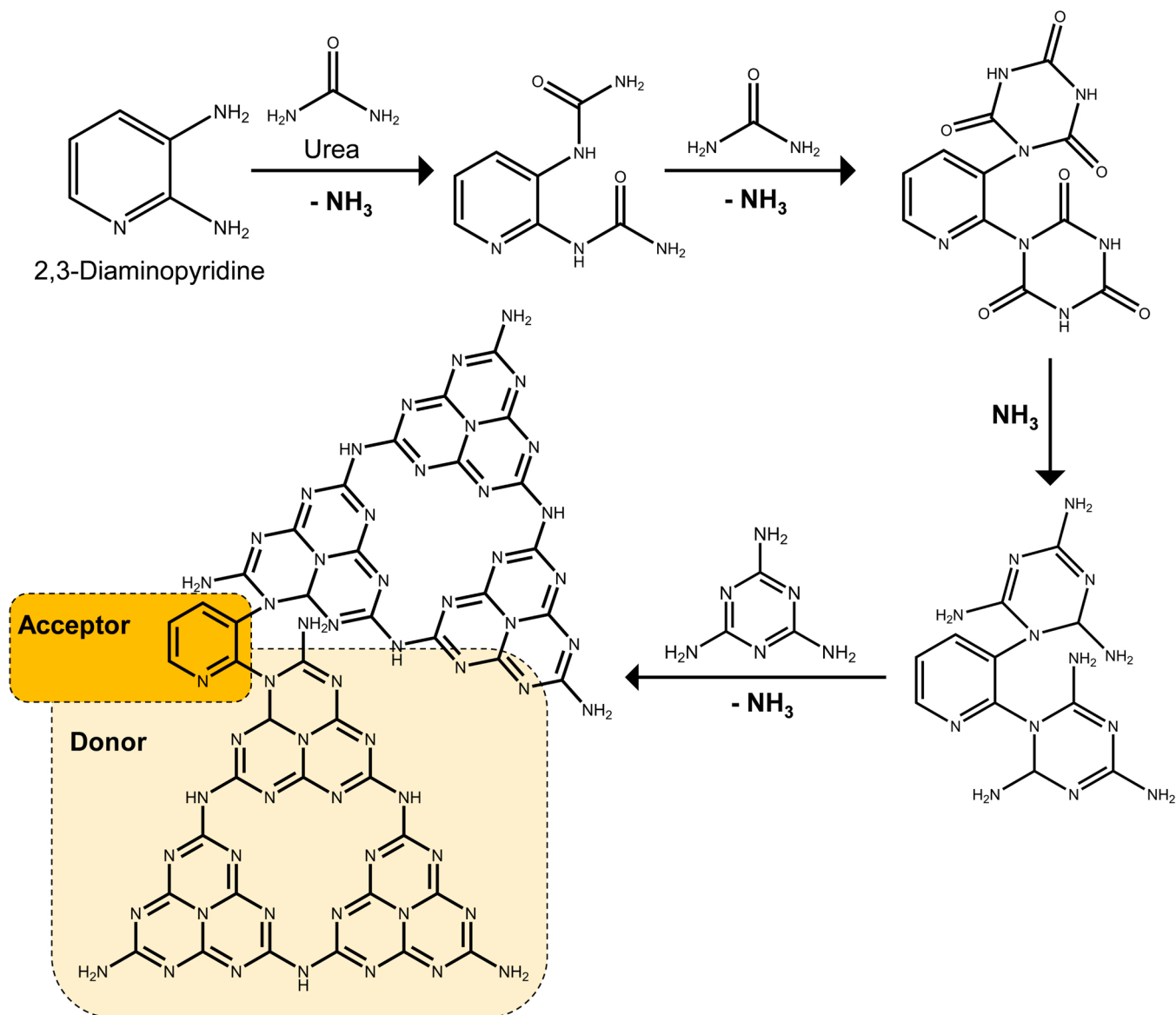

Scheme 1. Schematic illustration showing a plausible copolymerization of DAP with urea and melamine to form a D-π-A type network.

production. Among the prepared catalysts, 10DAPCN has maximum hydrogen generation activity of 26.24 mmolg^{-1}, compared to other synthesized 5DAPCN (12.65 mmolg^{-1}), and 20DAPCN (21.89 mmolg^{-1}) catalysts (Fig. 4a). Furthermore, the average hydrogen generation rate calculated for 10DAPCN (6.56 mmolg^{-1}h^{-1}) is 4.5 times higher than that of PCN (1.45 mmolg^{-1}h^{-1}) (Fig. 4b). The apparent quantum yield (AQY) of the 10DAPCN catalyst calculated at 420 nm is found to be 3.11% (Fig. S6). Remarkably, the photocatalytic hydrogen generation rate demonstrated in this work outperforms several state-of-art molecular-doped PCN-based, and metal free PCN and metal oxide-PCN based composites catalysts (refer to Fig. 4c, Table S2, and Table S3). Furthermore, the reusability of the 10DAPCN catalyst investigated by cyclic hydrogen generation experiment shown fairly good hydrogen generation for four consecutive cyclic experiment (Fig. S7). The excellent photoactivity of 10DAPCN catalyst for four consecutive cycles is likely from the structural stability of the 10DAPCN catalyst in aqueous medium. To gain more insights about the structural stability of catalyst, we recorded the FESEM images of 10DAPCN catalyst before and after photocatalytic reaction. The FESEM image of pristine 10DAPCN catalyst showed well-tact hollow tubular micro-assemblies with large surface-active sites indispensable for surface catalytic reaction. After photocatalytic reaction, the FESEM image revealed similar tubular microstructures with slight deformation of outer layers (Fig. S8a and b). This is likely from the surface bound hydrates formed by the interaction with water molecules. In a recent report, Zhang et al., realized anisotropic deformation of PCN nano structures triggered by the interaction of water molecules forming a hydrogen-bonded adsorption [41]. Furthermore, the XRD and FT-IR spectrum of 10DAPCN catalyst after photocatalytic reaction exhibited the similar characteristics features as that of fresh 10DAPCN catalyst (Fig. S8c and d), suggesting robust physico-chemical stability of 10DAPCN catalyst.

The photocatalytic RhB degradation experiment performed for pristine PCN shown 19% degradation after 30 min of visible light irradiation. While, all the DAP-doped PCN catalysts, 5DAPCN, 10DAPCN, and 20DAPCN shown enhanced photocatalytic degradation performance compared to PCN with degradation efficiency of 75%, 99%, and 78% after 30 min of light illumination, respectively (Fig. 4d). The degradation rate constant calculated by pseudo-first-order kinetics for PCN, 5DAPCN, 10DAPCN, and 20DAPCN catalysts are 0.006, 0.039, 0.086, and 0.043 min^{-1}, respectively (Fig. S9). Similar to the hydrogen production trend, the 10DAPCN catalyst exhibits the highest degradation efficiency when compared to pristine PCN. Furthermore, the RhB degradation performance of 10DAPCN was evaluated by reusing the catalyst for five consecutive degradation cycles, which demonstrated a negligible decrease in photocatalytic efficiency (Fig. 4e and S10a). The XRD pattern of the catalyst after the fifth cycle was also found to be consistent with the diffraction pattern of freshly prepared 10DAPCN catalyst (Fig. S10b). This result suggests the excellent structural stability of the as-prepared 10DAPCN catalyst during photocatalytic RhB degradation experiments.

To show the versatility of catalyst, an optimized 10DAPCN catalyst was further tested for degradation of various network-structured organic dyes such as anionic indigo carmine (IC), acid violet 7 (AV-7) and cationic methylene blue (MB), and malachite green (MG). The selected dyes have distinct network aromatic units, rigid structures, and are non-biodegradable. The photodegradation experiment exhibited that, 10DAPCN catalyst degrades 93% and 85% of anionic dyes IC and AV-7 after 20 min of light irradiation, respectively (Fig. 4f). However, photodegradation of cationic dyes MB and MG was found to be 57% and 12%, after 40 min of visible light irradiation. Relatively lower degradation of cationic dyes over 10DAPCN catalyst is likely from the network structure of dyes and possibly their lower interaction with the catalytic surface. The change in optical absorbance of dyes as a function of irradiation time is shown in Fig. S11a-e. In addition, when catalyst used for degradation of a mixture of cationic and anionic dye RhB and IC, 10DAPCN catalyst shown simultaneous degradation of both dyes (Fig. S11f). The degradation of widely used colorless antibiotic tetracycline hydrochloride (TCH) was also used as a model pollutant and 10DAPCN has shown 87% TCH degradation in 30 min of visible light irradiation (Fig. S12), which further evidence the strong
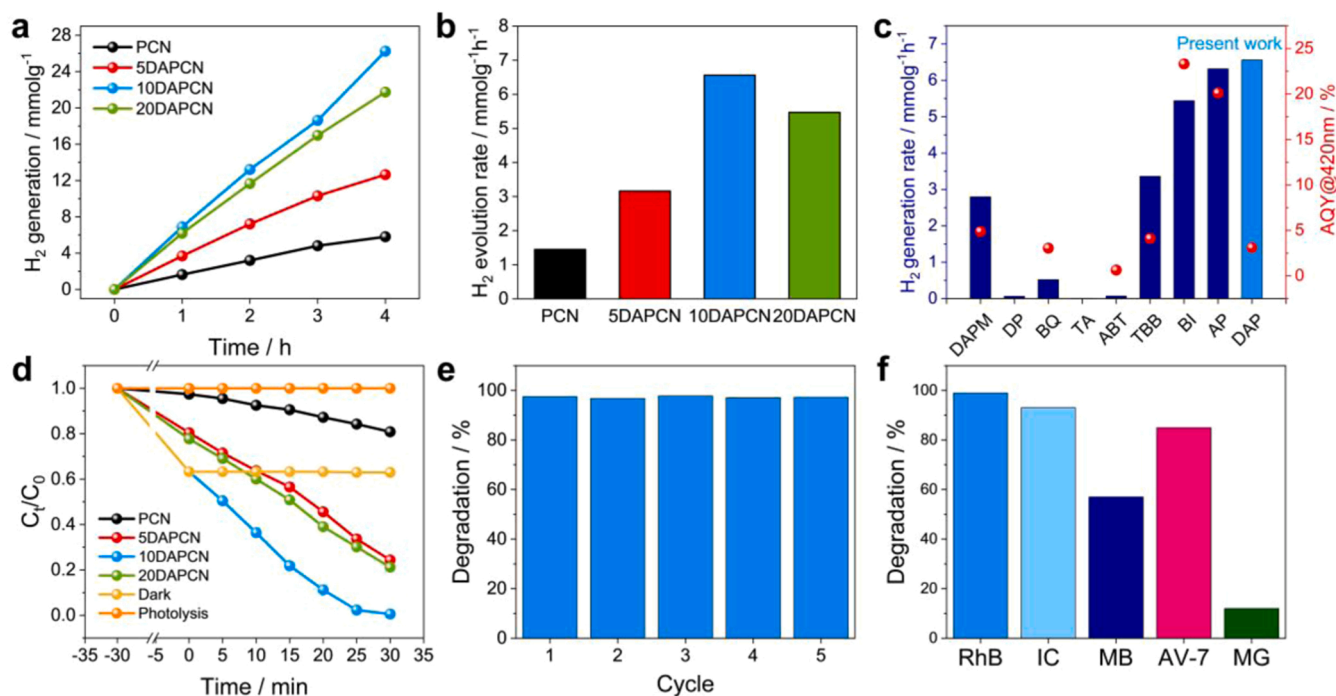
Fig. 4. Photocatalytic performance. (a) Amount of hydrogen generated as a function of time under visible light irradiation ($\lambda > 420$ nm), (b) photocatalytic hydrogen generation rate, (c) a comparison of hydrogen evolution rate and AQY at 420 nm of 10DAPCN catalyst with other state-of-art molecular doped PCN based catalysts, (d) photocatalytic rhodamine B (RhB) degradation performance of as-prepared catalysts, (e) recyclability test of 10DAPCN catalyst for RhB degradation, and (f) photocatalytic degradation of several organic-dyes with network structure by 10DAPCN catalyst.

photodegradation ability of 10DAPCN catalysts. These findings show that the as-prepared catalyst can be utilized for the degradation of various anionic and cationic dyes, a mixture of dyes, and even colorless antibiotic TCH.

3.4. Mechanistic insights for enhanced photoactivity

To understand the basis of DAP-doped PCN catalyst's enhanced photocatalytic activity, charge-carrier dynamics were initially examined using photoluminescence analysis. The photoluminescence (PL) spectra of the pristine PCN exhibits a strong PL emission peak at around 438 nm, which is attributed to the intrinsic LUMO to HOMO emission and a weak

shoulder peak at 460 nm is due to the charge transfer emission (Fig. 5a) [37]. In the case of 10DAPCN, these two peaks are remarkably redshifted in accordance with the UV-Vis absorption spectra, and quenching of emission peak is observed. The charge transfer emission peak in PCN is likely to arise owing to the transfer of electrons from electron-rich tertiary nitrogen to the tri-*s*-triazine ring in PCN [37]. Nevertheless, due to the low electron affinity of the tri-*s*-triazine ring than DAP, the possibility of this charge transition occurring is less and the pyridine ring of DAP is more likely to accept electrons due to its high electron affinity. In addition, due to distorted asymmetric planar structure, the excitons lose their energy due to the increase in the possibility of intramolecular collision, which resulted in PL quenching.
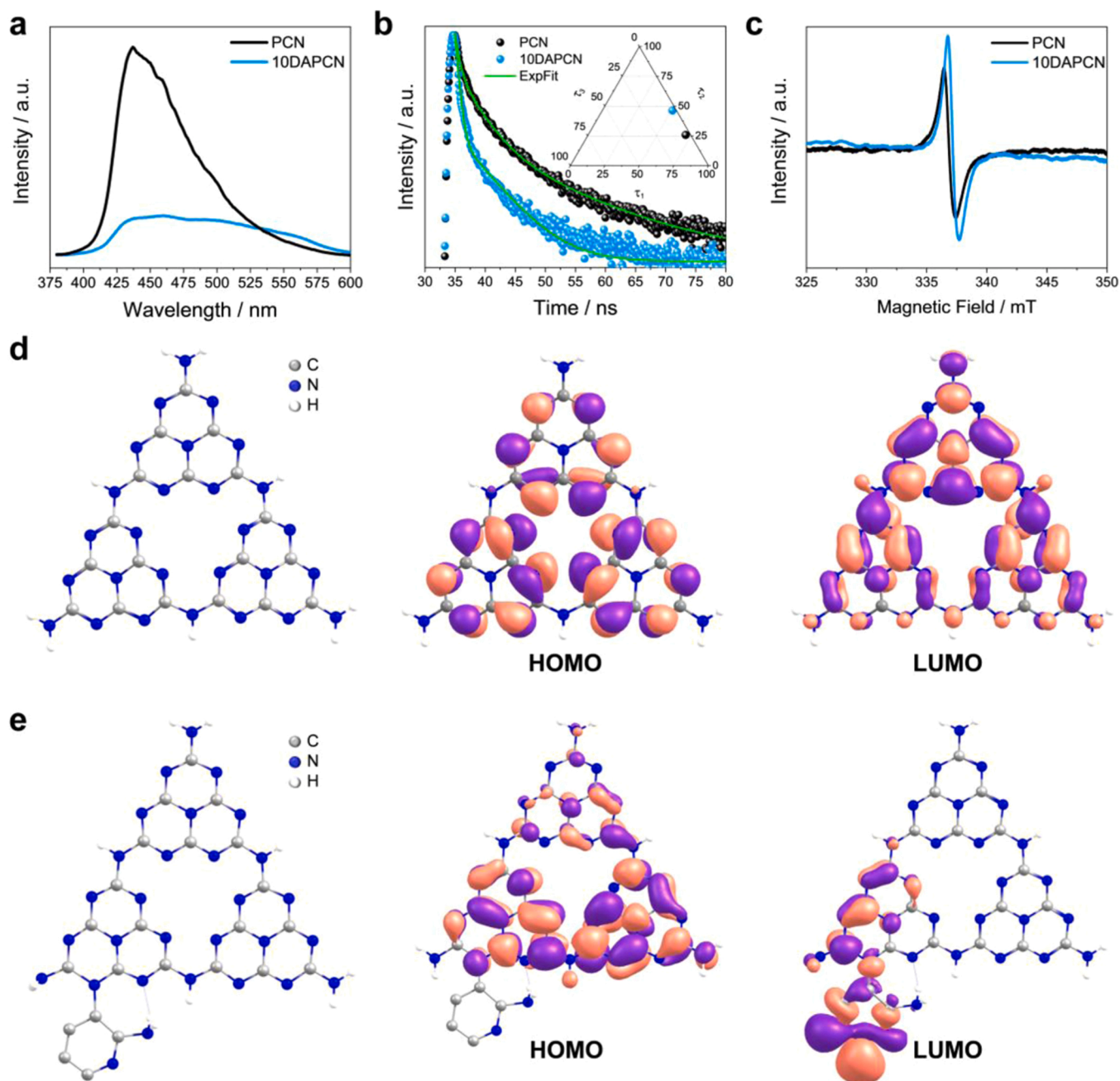
Fig. 5. Charge transfer dynamics in DAP-doped PCN structure and DFT analysis. (a) Steady-state photoluminescence (PL) spectra of PCN and 10DAPCN under 340 nm excitation, (b) time-resolved photoluminescence (TR-PL) spectra demonstrating reduced photoexcitons lifetime in 10DAPCN due to increase in non-radiative recombination, (The ternary diagram in the inset illustrations higher τ_2 intensity for 10DAPCN than PCN indicating the formation of stronger π-conjugated system) (c) electron spin resonance (ESR) spectrum of PCN and 10DAPCN, electronic structure with optimized HOMO and LUMO energy of (d) PCN and (e) DAPCN demonstrating reconstructed conjugated structure.

Furthermore, the time-resolved photoluminescence (TR-PL) decay spectroscopy was used to study the transfer mechanism of photo-excitons. The average fluorescence lifetime obtained for 10DAPCN (0.60 ns) is much smaller than that for PCN (1.62 ns) (Fig. 5b). Remarkably, all three positive decay components τ_1, τ_2, and τ_3 of 10DAPCN are smaller than those for PCN indicating 10DAPCN has an effective charge transfer process and higher charge carrier mobility than PCN due to faster non-radiative recombination of photogenerated charge carriers (Table S4) [42]. Further to note, the fractional intensity of τ_2 for 10DAPCN is 46.3% which is higher than that for PCN (25.8%) indicating that the excited electrons in 10DAPCN mainly exists in the π * , which suggests stronger π-conjugated system than PCN counterpart (inset of Fig. 5b) [43]. The quenched PL spectrum also supports a low probability of radiative recombination in 10DAPCN catalyst. The quenching of emission peak and a lower lifetime of photoexcitons in 10DAPCN demonstrates that the recombination of photogenerated charge carriers is greatly suppressed after doping. The electronic band structure of PCN and 10DAPCN catalysts was further studied by electron paramagnetic resonance (EPR) spectra, which shown an EPR peak centered at a g-value of 2.0008 (Fig. 5c). The peak corresponds to the delocalized unpaired electrons on the sp^2 carbon atom in the π-conjugated aromatic tri-s-triazine ring. Remarkably, the EPR signal intensity of the 10DAPCN catalyst was stronger than the PCN counterpart, which indicates generation of more delocalized electrons and increased density/concentration of unpaired electrons [44]. The enhancement is attributed to the rearrangement of π-electrons due to formation of D-π-A structure and extended π-conjugated system due to the incorporation of DAP rings. The transient photocurrent measurement further revealed enhance photocurrent intensity for 10DAPCN compared to PCN (Fig. S13). These result reveals that electronic band structure of DAP-doped PCN increases charge carrier mobility and achieves efficient separation of photoexcitons.

The textural feature of the as-prepared catalyst determined by the N_2 adsorption-desorption isotherm reveals that the Brunauer-Emmett-Teller (BET) surface area of 10DAPCN catalyst is 138.92 m^{2}g^{-1}, which is nearly 12-times higher than the pristine PCN (13.04 m^{2}g^{-1}) (Fig. S14a). The Barrett-Joyner-Halenda (BJH) pore volume and pore radius are also found to be large for the 10DAPCN catalyst (Fig. S14b and Table 1). The enhancement in the active surface area of the 10DAPCN is corroborated to the alteration in the primary polymeric structure due to the incorporation of DAP moieties in between tri-s-triazine monomeric units of PCN. It is obvious that the surface photocatalytic reactions such as hydrogen production and dye degradation are directed by the availability of active surface area [45]. Therefore, the large active surface area of 10DAPCN compared to PCN implies that photo-redox reactions occur at a faster rate on the 10DAPCN catalyst surface. All these results suggest that the incorporation of DAP in PCN scaffolds promotes the facile dissociation of photoexcitons and improves textural features of PCN.

To further elucidate the effect of incorporating π-deficient nitrogenous DAP moiety into the PCN framework for efficient catalytic behavior, the hydrogen adsorption mechanism was evaluated using electronic structure calculations. The computed band gap using the HSE06 hybrid functional is found to be 2.64 and 2.51 eV for PCN and DAPCN, respectively, which is in agreement with the experimental

values. The introduction of DAP into PCN reduces the bandgap because of the sudden shift in the energy level and thereby enhancing the photocatalytic activity. To understand the electron distribution, we computed the HOMO and LUMO energy levels of the optimized PCN and DAPCN structure. The HOMO of PCN is mainly comprised of the combination of nitrogen p_z orbitals and the LUMO is mainly dominated by C-N bond orbitals on the same PCN unit (Fig. 5d). The HOMO and LUMO located on the same PCN unit encourage rapid recombination of photoexcitons. While, in case of DAPCN, the incorporation of DAP molecule onto the PCN structure significantly relocates the π-conjugated electrons to modify the relative HOMO and LUMO energy levels. Here, the HOMO of DAPCN is mainly concentrated on the PCN framework, while the LUMO is distributed over the pyridine ring of DAP, which can effectively reduce rapid recombination of charge carriers and boost photoactivity (Fig. 5e). In addition, the orbital shape clearly indicates an efficient intramolecular charge transfer from HOMO to LUMO in the DAPCN structure from donor to acceptor unit. Furthermore, the introduction of DAP molecule shifts up the HOMO from − 4.96 to − 4.88 eV, while the LUMO shifts down from − 2.32 to − 2.37 eV (Fig. 6a). This results in the reduction of energy gap of DAPCN by 0.13 eV compared to that of PCN, which is in accordance with the experimental results. Also, it indicates energetically easier ICT transition in the D-π-A complex. Typically, the performance of a hydrogen evolving catalyst depends on the ability to adsorb hydrogen intermediates (H*), which can be obtained by analyzing the adsorption free energy of H* (ΔG_{H*}). Fig. 6b represents the Gibbs free energy change profile of H* adsorbed on pure PCN and DAPCN. Accordingly, the ΔG_H value close to zero represents better catalytic activity, while the negative and positive values indicate easy and tough adsorption of protons, on the surface of a catalyst, respectively. Here, the hydrogen binding energy is more negative for pure PCN (−0.49 eV), which restricts the hydrogen generation due to remarkably suppressed desorption of hydrogen intermediates. The catalytic activity of DAPCN is significantly enhanced after the introduction of DAP, where the hydrogen adsorption on the DAPCN surface is reduced to − 0.11 eV, which is much closer to the optimal value ($\Delta G_{H*} = 0$). Overall, the reduced bandgap, enhanced visible light absorption, optimal ΔG_{H*} value of DAPCN leads to the exceptional catalytic behavior of DAPCN, thereby accelerating the significant hydrogen production.

Further, to understand the mechanism of hydrogen generation and degradation of organics, the conduction band (CB) and valence band (VB) potentials of PCN and 10DAPCN have been determined using the Mulliken Electronegativity equation (Eqs. 4 and 5);

$$E_{CB} = \chi - 0.5 \ E_g - E_e \tag{4}$$

$$E_{VB} = E_{CB} + E_g \tag{5}$$

where, E_{CB} and E_{VB}, are the CB and VB potentials in eV respectively, χ is the absolute electronegativity (geometric mean of absolute electronegativity of constituent atoms; 4.72 for carbon nitride semiconductor), [46] E_e is the energy of free electrons (E_e= 4.5 eV vs. NHE), and E_g is the bandgap of the semiconductor catalyst (2.77 and 2.64 eV for PCN and 10DAPCN, respectively).

The CB and VB position of pristine PCN is calculated to be − 1.16 eV and + 1.61 eV, respectively. Notably, a remarkable shift in CB and VB position to − 1.10 eV and + 1.54 eV is observed for the 10DAPCN catalyst. Despite the positive shift in the conduction band edge potential, the required potential to drive two electron, proton reduction reaction to generate hydrogen is satisfied for the DAP-doped PCN catalyst. As shown in Fig. 6c, on light irradiation, electrons are excited to CB, and holes are generated in the VB of DAP-doped PCN catalyst. The photoexcited electrons are then withdrawn by pyridine rings from the PCN core thereby improving the separation efficiency of photoexcitons. The photogenerated electrons then reduce the water molecules adsorbed on surface catalytic sites to generated hydrogen. Meanwhile, the photogenerated holes remain on the PCN core and are consumed by TEOA in

Table 1
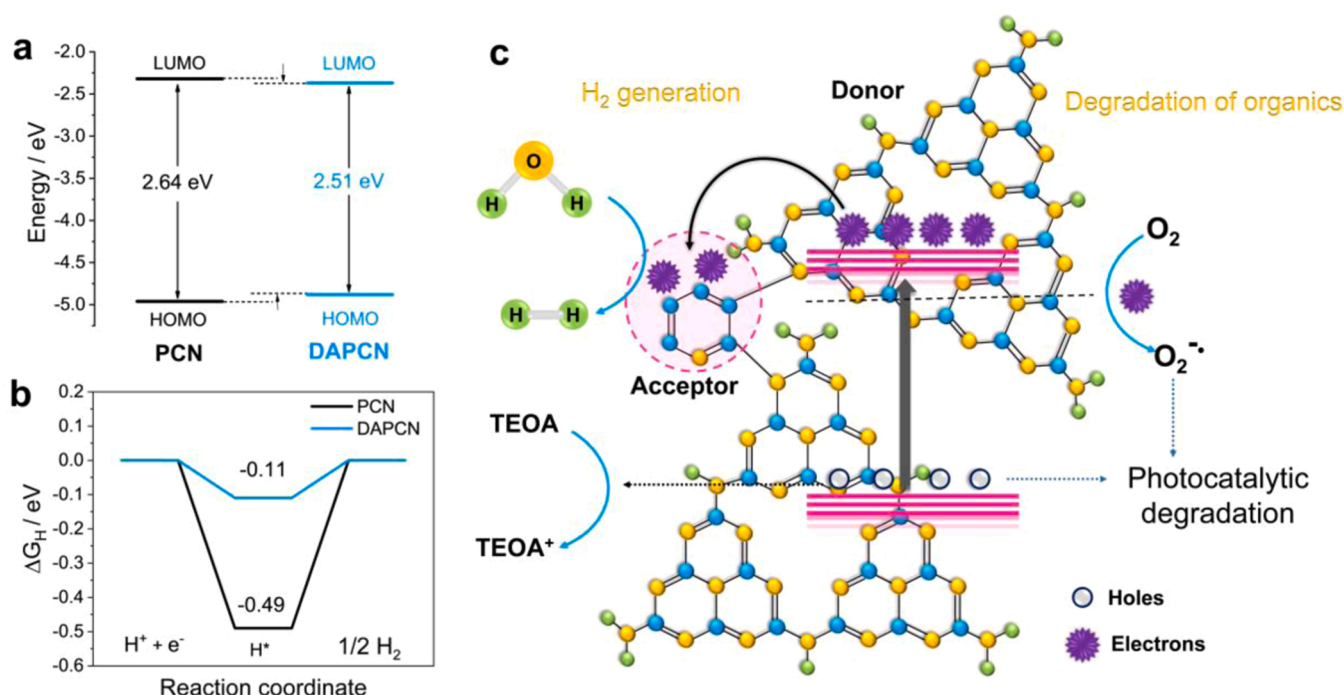Physicochemical properties of as-prepared PCN and 10DAPCN sample.

Sample	$E_g{}^a$ (eV)	$S_{BET}{}^b$ (m^{2}g^{-1})	$D_v{}^c$ (cm^{3}g^{-1})	$D_r{}^d$ (nm)
PCN	2.77	13.04	0.0188	1.06
10DAPCN	2.64	138.92	0.1795	1.41

[a] Bandgap energy estimated from KM plot.
[b] BET surface area obtained from nitrogen adsorption-desorption isotherm.
[c] BJH pore volume.
[d] BJH pore radius.

Fig. 6. (a) Optimized HOMO and LUMO band gap structure of PCN and DAPCN, (b) free-energy reaction coordinate diagram representing the relative hydrogen adsorption free-energy for PCN and DAPCN, indicating that hydrogen binding energy of DAPCN close to zero is more feasible to desorb hydrogen intermediates than its PCN counterpart, and (c) Schematic illustration showing photocatalytic hydrogen generation and degradation of organic pollutants over DAPCN catalyst.

solution. Further, in the case of degradation of organics, a charge trapping experiment revealed that superoxide radicals ($O_2^{-\bullet}$), and holes are the reactive oxidative species (ROS) which play a vital role in the degradation of dye molecules (Fig. S15). The CB of DAP-doped PCN provides enough negative potential ($O_2/O_2^{-\bullet} = -0.046$ eV vs. NHE) to generate the superoxide radical anions and drive the photocatalytic degradation reaction. On the other hand, holes directly participate in photodegradation reactions. Henceforth, the formation of the D-π-A structure is a promising strategy to improve the photocatalytic activity of pristine PCN by modulating textural features and optoelectronic properties.

4. Conclusions

In summary, we have successfully constructed a PCN-based D-π-A type network by incorporating N-rich π-deficient DAP moieties following the copolymerization approach. The D-π-A type network demonstrates extended visible light response with the formation of the ICT band. The ICT band arises due to the transfer of photogenerated electrons from PCN (donor) to pyridine rings of DAP (acceptor). Meanwhile, the network shows faster non-radiative recombination of photoexcitons with an average lifetime of 0.60 ns. Almost 4.5 times higher photocatalytic hydrogen generation is realized for 10DAPCN as compared to PCN and higher dye degradation kinetics under visible light irradiation. This enhanced photocatalytic behavior is attributed to the synergistic effect of the higher surface area, availability of more visible light active sites, and excellent charge transfer dynamics. The proposed metal-free strategy aspires to modify PCN by constructing D-π-A networks using electron-accepting π − conjugated organic compounds that regulate the charge transfer pathways.

CRediT authorship contribution statement

Toshali Bhoyar: Conceptualization, Data curation, Investigation, Methodology, Visualization, Writing – original draft. **Dong Jin Kim:** Investigation, Validation. **B. Moses Abraham:** Investigation, Data curation, Writing – review & editing. **Surendar Tonda:** Investigation, Formal analysis. **Nilesh R. Manwar:** Investigation, Writing – review & editing. **Devthade Vidyasagar:** Conceptualization, Data curation, Methodology, Visualization, Writing – review & editing, Supervision. **Suresh S. Umare:** Investigation, Visualization, Resources, Validation, Writing – review & editing, Supervision, and Funding acquisition.

Declaration of Competing Interest

The authors declare that they have no known competing financial interests or personal relationships that could have appeared to influence the work reported in this paper.

Acknowledgments

Appendix A. Supporting information

Supplementary data associated with this article can be found in the online version at doi:10.1016/j.apcatb.2022.121347.

References

[1] X. Wang, K. Maeda, A. Thomas, K. Takanabe, G. Xin, J.M. Carlsson, K. Domen, M. Antonietti, A metal-free polymeric photocatalyst for hydrogen production from water under visible light, Nat. Mater. 8 (2009) 76–80.

[2] G. Dong, L. Zhang, Porous structure dependent photoreactivity of graphitic carbon nitride under visible light, J. Mater. Chem. 22 (2012) 1160–1166.

[3] V. Devthade, A. Gupta, S.S. Umare, Graphitic carbon nitride– γ-gallium oxide (GCN-γ-Ga$_2$O$_3$) nanohybrid photocatalyst for dinitrogen fixation and pollutant decomposition, ACS Appl. Nano Mater. 1 (2018) 5581–5588.

[4] Y. Cui, Y. Tang, X. Wang, Template-free synthesis of graphitic carbon nitride hollow spheres for photocatalytic degradation of organic pollutants, Mater. Lett. 161 (2015) 197–200.

[5] L. Lin, Z. Yu, X. Wang, Crystalline carbon nitride semiconductors for photocatalytic water splitting, Angew. Chem. Int. Ed. 58 (2019) 6164–6175.

[6] K. Li, W.-D. Zhang, Creating graphitic carbon nitride based Donor-π–Acceptor-π–Donor structured catalysts for highly photocatalytic hydrogen evolution, Small 14 (2018), 1703599.

[7] Z. Lin, X. Wang, Nanostructure engineering and doping of conjugated carbon nitride semiconductors for hydrogen photosynthesis, Angew. Chem. 125 (2013) 1779–1782.

[8] D. Vidyasagar, S.G. Ghugal, S.S. Umare, M. Banavoth, Extended π-conjugative n-p type homostructural graphitic carbon nitride for photodegradation and charge-storage applications, Sci. Rep. 9 (2019) 1–10.

[9] J. Zhang, G. Zhang, X. Chen, S. Lin, L. Möhlmann, G. Dołęga, G. Lipner, M. Antonietti, S. Blechert, X. Wang, Co-monomer control of carbon nitride semiconductors to optimize hydrogen evolution with visible light, Angew. Chem. Int. Ed. 51 (2012) 3183–3187.

[10] Z. Chen, P. Sun, B. Fan, Q. Liu, Z. Zhang, X. Fang, Textural and electronic structure engineering of carbon nitride via doping with π-deficient aromatic pyridine ring for improving photocatalytic activity, Appl. Catal. B 171 (2015) 10–16.

[11] J. Zhang, M. Zhang, S. Lin, X. Fu, X. Wang, Molecular doping of carbon nitride photocatalysts with tunable bandgap and enhanced activity, J. Catal. 310 (2014) 24–30.

[12] Q. Cui, J. Xu, X. Wang, L. Li, M. Antonietti, M. Shalom, Phenyl-modified carbon nitride quantum dots with distinct photoluminescence behavior, Angew. Chem. Int. Ed. 55 (2016) 3672–3676.

[13] H. Kim, S. Gim, T.H. Jeon, H. Kim, W. Choi, Distorted carbon nitride structure with substituted benzene moieties for enhanced visible light photocatalytic activities, ACS Appl. Mater. Interfaces 9 (2017) 40360–40368.

[14] D. Vidyasagar, N. Manwar, A. Gupta, S.G. Ghugal, S.S. Umare, R. Boukherroub, Phenyl-grafted carbon nitride semiconductor for photocatalytic CO$_2$-reduction and rapid degradation of organic dyes, Catal. Sci. Technol. 9 (2019) 822–832.

[15] N. Banerji, G. Angulo, I. Barabanov, E. Vauthey, Intramolecular charge-cransfer dynamics in covalently linked perylene−dimethylaniline and cyanoperylene−dimethylaniline, J. Phys. Chem. A 112 (2008) 9665–9674.

[16] C. Zhu, T. Wei, Y. Wei, L. Wang, M. Lu, Y. Yuan, L. Yin, L. Huang, Unravelling intramolecular charge transfer in donor–acceptor structured g-C$_3$N$_4$ for superior photocatalytic hydrogen evolution, J. Mater. Chem. A 9 (2021) 1207–1212.

[17] X. Zong, L. Niu, W. Jiang, Y. Yu, L. An, D. Qu, X. Wang, Z. Sun, Constructing creatinine-derived moiety as donor block for carbon nitride photocatalyst with extended absorption and spatial charge separation, Appl. Catal. B 291 (2021), 120099.

[18] Z. Li, S. Zhou, Q. Yang, Z. Zhang, X. Fang, Insight into the enhanced hydrogen evolution activity of 2, 4-diaminopyrimidine-doped graphitic carbon nitride photocatalysts, J. Phys. Chem. C 123 (2019) 2228–2237.

[19] C. Zhou, G. Zeng, D. Huang, Y. Luo, M. Cheng, Y. Liu, W. Xiong, Y. Yang, B. Song, W. Wang, B. Shao, Z. Li, Distorted polymeric carbon nitride via carriers transfer bridges with superior photocatalytic activity for organic pollutants oxidation and hydrogen production under visible light, J. Hazard. Mater. 386 (2020) 121947.

[20] X. Lin, X. Hou, L. Cui, S. Zhao, H. Bi, H. Du, Y. Yuan, Increasing π-electron availability in benzene ring incorporated graphitic carbon nitride for increased photocatalytic hydrogen generation, J. Mater. Sci. Technol. 65 (2021) 164–170.

[21] W.-K. Jo, S. Moru, S. Tonda, Magnetically responsive SnFe$_2$O$_4$/g-C$_3$N$_4$ hybrid photocatalysts with remarkable visible-light-induced performance for degradation of environmentally hazardous substances and sustainable hydrogen production, Appl. Surf. Sci. 506 (2020), 144939.

[22] P.E. Blöchl, Projector augmented-wave method, Phys. Rev. B 50 (1994) 17953.

[23] J.P. Perdew, K. Burke, M. Ernzerhof, Generalized gradient approximation made simple, Phys. Rev. Lett. 77 (1996) 3865–3868.

[24] B.M. Abraham, Adsorption behavior of explosive molecules on g-C$_3$N$_4$ nanostructure: a novel approach for sensing energetic materials, J. Phys. Chem. Solids 149 (2021), 109777.

[25] E. Skúlason, V. Tripkovic, M.E. Björketun, S. Gudmundsdóttir, G. Karlberg, J. Rossmeisl, T. Bligaard, H. Jónsson, J.K. Nørskov, Modeling the electrochemical hydrogen oxidation and evolution reactions on the basis of density functional theory calculations, J. Phys. Chem. C 114 (2010) 18182–18197.

[26] B.-w Sun, H.-y Yu, Y.-j Yang, H.-j Li, C.-y Zhai, D.-J. Qian, M. Chen, New complete assignment of X-ray powder diffraction patterns in graphitic carbon nitride using discrete Fourier transform and direct experimental evidence, Phys. Chem. Chem. Phys. 19 (2017) 26072–26084.

[27] J. Zhang, X. Chen, K. Takanabe, K. Maeda, K. Domen, J.D. Epping, X. Fu, M. Antonietti, X. Wang, Synthesis of a carbon nitride structure for visible-light catalysis by copolymerization, Angew. Chem. Int. Ed. 49 (2010) 441–444.

[28] Z. Jin, X. Jiang, Q. Zhang, S. Huang, L. Zhang, L. Huang, T. He, H. Zhang, T. Ohno, S. Ruan, Infrared response in photocatalytic polymeric carbon nitride for water splitting via an upconversion mechanism, Commun. Mater. 1 (2020) 1–10.

[29] C. Li, H. Wu, D. Zhu, T. Zhou, M. Yan, G. Chen, J. Sun, G. Dai, F. Ge, H. Dong, High-efficient charge separation driven directionally by pyridine rings grafted on carbon nitride edge for boosting photocatalytic hydrogen evolution, Appl. Catal. B 297 (2021), 120433.

[30] P. Niu, L. Zhang, G. Liu, H.M. Cheng, Graphene-like carbon nitride nanosheets for improved photocatalytic activities, Adv. Funct. Mater. 22 (2012) 4763–4770.

[31] X. Wang, J. Meng, X. Zhang, Y. Liu, M. Ren, Y. Yang, Y. Guo, Controllable approach to carbon-deficient and oxygen-doped graphitic carbon nitride: robust photocatalyst against recalcitrant organic pollutants and the mechanism insight, Adv. Funct. Mater. 31 (2021), 2010763.

[32] H.Y. Yuan, J.Y. Bai, B. Xu, X.Y. Li, S.Y. Xiao, P.F. Liu, X.L. Wang, H.G. Yang, Graphite carbon nitride doped with a benzene ring for enhanced photocatalytic H$_2$ evolution, Chem. Commun. 57 (2021) 3042–3045.

[33] T. Kondo, D. Guo, T. Shikano, T. Suzuki, M. Sakurai, S. Okada, J. Nakamura, Observation of Landau levels on nitrogen-doped flat graphite surfaces without external magnetic fields, Sci. Rep. 5 (2015) 16412.

[34] C. Zhou, G. Zeng, D. Huang, Y. Luo, M. Cheng, Y. Liu, W. Xiong, Y. Yang, B. Song, W. Wang, Distorted polymeric carbon nitride via carriers transfer bridges with superior photocatalytic activity for organic pollutants oxidation and hydrogen production under visible light, J. Hazard. Mater. 386 (2020), 121947.

[35] F. Yang, G. Ba, Z. Wang, H. Li, Surface modification induced construction of core-shell homojunction of polymeric carbon nitride for boosted photocatalytic performance, J. Colloid Interface Sci. (2021).

[36] G. Zhang, A. Savateev, Y. Zhao, L. Li, M. Antonietti, Advancing the n → π* electron transition of carbon nitride nanotubes for H$_2$ photosynthesis, J. Mater. Chem. A 5 (2017) 12723–12728.

[37] X. Fan, L. Zhang, R. Cheng, M. Wang, M. Li, Y. Zhou, J. Shi, Construction of graphitic C$_3$N$_4$-based intramolecular donor–acceptor conjugated copolymers for photocatalytic hydrogen evolution, ACS Catal. 5 (2015) 5008–5015.

[38] H. Fattahimoghaddam, T. Mahvelati-Shamsabadi, B.-K. Lee, Enhancement in photocatalytic H$_2$O$_2$ production over g-C$_3$N$_4$ nanostructures: a collaborative approach of nitrogen deficiency and supramolecular precursors, ACS Sustain. Chem. Eng. 9 (2021) 4520–4530.

[39] Y. Zhang, Z. Huang, C.-L. Dong, J. Shi, C. Cheng, X. Guan, S. Zong, B. Luo, Z. Cheng, D. Wei, Synergistic effect of nitrogen vacancy on ultrathin graphitic carbon nitride porous nanosheets for highly efficient photocatalytic H$_2$ evolution, Chem. Eng. J. 431 (2022), 134101.

[40] H. Zhang, Y. Xi, C. Su, Z.G. Liu, Lab study of urea deposit formation and chemical transformation process of diesel after treatment system, SAE Technical Paper (2017).

[41] Y. Zhang, Y. Song, Y. Shen, K. Chen, Q. Zhou, Y. Lv, H. Yang, E. Xu, S. Liu, L. Liu, Water molecule-triggered deformation of carbon nitride nanoribbons enabling contactless respiratory inspection, CCS Chem. 3 (2021) 1615–1625.

[42] C. Li, H. Wu, D. Zhu, T. Zhou, M. Yan, G. Chen, J. Sun, G. Dai, F. Ge, H. Dong, High-efficient charge separation driven directionally by pyridine rings grafted on carbon nitride edge for boosting photocatalytic hydrogen evolution, Appl. Catal. B (2021), 120433.

[43] P. Zhang, L.-J. Wu, W.-G. Pan, Z.-Z. Wei, X.-Y. Liang, R.-T. Guo, Granular polymeric carbon nitride with carbon vacancies for enhanced photocatalytic hydrogen evolution, Sol. RRL 5 (2021), 2000796.

[44] N. Banerji, G. Angulo, I. Barabanov, E. Vauthey, Intramolecular charge-transfer dynamics in covalently linked perylene− dimethylaniline and cyanoperylene− dimethylaniline, J. Phys. Chem. A 112 (2008) 9665–9674.

[45] Y. Wang, S. Zhao, Y. Zhang, W. Chen, S. Yuan, Y. Zhou, Z. Huang, Synthesis of graphitic carbon nitride with large specific surface area via copolymerizing with nucleobases for photocatalytic hydrogen generation, Appl. Surf. Sci. 463 (2019) 1–8.

[46] Y. Che, Q. Liu, B. Lu, J. Zhai, K. Wang, Z. Liu, Plasmonic ternary hybrid photocatalyst based on polymeric g-C$_3$N$_4$ towards visible light hydrogen generation, Sci. Rep. 10 (2020) 1–12.